Direct Imaging of the Defect-Mediated Magnetic Phase Transition in a Topological Superlattice $MnSb_6Te_{10}$

Xiaotian Yang(杨笑天)[1,†], Zijian Guo(郭子健)[1,†], Binshuo Zhang(张滨朔)[1,†]
Chao Dong(董超)[2], Wei Xia(夏威)[1,3], Yanfeng Guo(郭艳峰)[1,3], and Wenbo Wang(王文波)[1,3*]
[1]State Key Laboratory of Quantum Functional Materials,
School of Physical Science and Technology, ShanghaiTech University,
Shanghai 201210, China
[2]Wuhan National High Magnetic Field Center,
Huazhong University of Science and Technology, Wuhan 430074, China
[3]ShanghaiTech Laboratory for Topological Physics, Shanghai 201210, China
[†]These authors contribute equally to this work: Xiaotian Yang, Zijian Guo and Binshuo Zhang

Abstract

Structural disorder, specifically cation site-mixing, fundamentally dictates the magnetic energy landscape of van der Waals topological insulators. In this work, we resolve the real-space dynamics of the temperature-driven ferromagnetic (FM) to antiferromagnetic (AFM) phase transition in the superlattice $MnSb_6Te_{10}$. We demonstrate that Mn_{Sb} antisite defects introduce competing interlayer exchange pathways, which trap the system in a metastable FM state at low temperatures. Using cryogenic magnetic force microscopy (MFM), we reveal that this state relaxes upon warming not through homogeneous melting, but via first-order spatial fragmentation into microscale magnetic islands, eventually yielding the intrinsic AFM ground state. Monte Carlo simulations based on a spatially inhomogeneous Heisenberg model reproduce these fragmentation dynamics, identifying defect density as a deterministic control knob for the magnetic phase competition. These results provide a comprehensive nanoscale picture of defect-modulated spin textures, establishing structural site-mixing as a viable strategy for manipulating magnetic symmetry and engineering non-trivial topological phases.

Keywords

metastable ferromagnetism, magnetic defects, phase transition, magnetic force microscopy

*Corresponding author. E-mail: wangwb1@shanghaitech.edu.cn

PACS

64.60.My, 75.30.Hx , 75.30.Kz , 68.37.Rt

1. Introduction

The discovery of magnetic topological insulators (MTIs) provides a fertile platform for investigating novel quantum phenomena, such as the quantum anomalous Hall effect (QAHE), axion insulating states, and magnetic Weyl semimetals [1–4]. Recently, the van der Waals (vdW) layered family $Mn(Bi,Sb)_2Te_4$ has attracted considerable interest due to its interlocking topological bands and intrinsic magnetic order [5–9]. In an ideal stoichiometric lattice, these compounds typically stabilize in an A-type antiferromagnetic (AFM) ground state, where adjacent magnetic septuple layers (SLs) are coupled antiferromagnetically, yielding a compensated global net moment.

However, the intrinsic interlayer AFM coupling in these materials gives rise to highly complex magnetic orders, making it difficult to maintain magnetic moments in the out-of-plane direction. Because a robust out-of-plane magnetization at zero magnetic field is a strict prerequisite for the QAHE, stabilizing a robust QAHE in these intrinsic magnetic topological materials remains a major challenge [4,10,11]. Consequently, introducing an out-of-plane ferromagnetic (FM) order into the system is essential to overcome this limitation. To address this bottleneck, a superlattice strategy has been implemented by inserting non-magnetic $(Bi,Sb)_2Te_3$ quintuple layers (QLs) as insulating spacers. This structural modulation effectively increases the interlayer distance, causing the native interlayer AFM coupling to decay as a function of the spacer thickness [8,12–15].

While this spacer engineering successfully weakens the host interlayer AFM interaction, it concurrently establishes a highly competitive magnetic energy landscape that is sensitive to structural disorder. Due to the chemical similarity between Mn and Sb, substantial cation antisite defects Mn_{Sb} can form during crystal growth, acting as local interlayer exchange pathways that introduce competing FM exchange channels to modify the low-temperature magnetic state [13,16–21]. Because the energy barrier between these competing configurations is small [14], this defect-induced FM order is thermally volatile, leading to a spontaneous transition back to the AFM state upon warming [22–26]. Currently, investigations of this defect-driven phase evolution rely primarily on bulk-averaged magnetometry, which spatially integrates the signal and blurs the local spin textures governed by spatial fluctuations in defect density. Therefore, it is imperative to utilize direct real-space imaging techniques to capture the nanoscale evolution of the ferromagnetic to antiferromagnetic phase transition driven by thermal fluctuations [27].

Here, we combine high-field pulsed magnetization measurements, cryogenic magnetic force microscopy (MFM), and Monte Carlo (MC) simulations to resolve how a field-prepared metastable FM state relaxes into the AFM ground state in the vdW superlattice $MnSb_6Te_{10}$. High-field pulsed magnetization reveals an effective ferrimagnetic configuration driven by antisite mixing defects. Furthermore, real-space MFM imaging directly confirms the presence of this metastable FM state, demonstrating that it is reversibly

switchable under small magnetic fields. During zero-field warming, rather than melting homogeneously, this state fragments into smaller magnetic regions before the detectable stray-field contrast disappears —a process consistent with relaxation toward a compensated AFM state. MC simulations reproduce this qualitative behavior within a spatially inhomogeneous exchange model, establishing defect-mediated metastability as the microscopic origin of the observed FM-to-AFM phase transition.

2. Competitive exchange coupling

$MnSb_6Te_{10}$ crystallizes in a layered vdW superlattice geometry, where the primary unit cell consists of alternating stackings of one magnetic [$MnSb_2Te_4$] septuple layer [SL, (Te−Sb−Te−Mn−Te−Sb−Te)] and two non-magnetic [Sb_2Te_3] quintuple layers [QL, (Te−Sb−Te−Sb−Te)] [14,25,26]. Within the SL block, the local magnetic moments of individual Mn ions align parallel to each other due to the intralayer ferromagnetic exchange interaction ($J_{\mathrm{FM}}^{\mathrm{intra}}$). Ideally, adjacent SLs are coupled via a weak, long-range interlayer van der Waals exchange path dominated by an antiferromagnetic interaction (J_{AFM}^{1}), yielding a conventional A-type AFM arrangement as schematically illustrated in Fig. 1a, where black arrows denote the equilibrium spin directions along the c-axis.

However, the interlayer magnetic exchange in this lattice is highly susceptible to local perturbations from cation site mixing. As shown in Fig. 1b, this structural disorder manifests as Mn_{Sb} antisite defects [16–19,28–30], where a fraction of Mn ions vacate the host main layer (Mn_{Mn}) to substitute native Sb sites within the lattice spacer. These Mn_{Sb} ions fundamentally alter the local exchange network by introducing competing interlayer coupling channels: a local antiferromagnetic interaction (J_{AFM}^{2}) between host Mn_{Mn} spins and interlayer Mn_{Sb} defects, and a short-range ferromagnetic interaction (J_{FM}^{3}) between neighboring Mn_{Sb} defects. Together, these defect-mediated pathways encourage the Mn_{Mn} moments to align ferromagnetically across the vdW gaps. Once a critical defect density is surpassed, these emergent FM interactions overpower the pristine interlayer AFM coupling (J_{AFM}^{1}). Because the intralayer FM coupling strongly dominates over the interlayer interactions, the atomic-scale coexistence of FM and AFM phases is suppressed; consequently, neighboring septuple layers lock into a parallel alignment, ensuring the formation of a globally uniform FM state at low temperatures.

Low-field isothermal magnetization M–H loops parallel to the c-axis reveal a distinct temperature-driven transition from a low-temperature FM state to a high-temperature AFM ground state in Fig. 1c. At 2 K, the system exhibits a magnetic hysteresis loop with a coercive field of ~ 0.02 T. Upon warming past 4 K, the hysteresis loop systematically contracts and closes, marking the disappearance of the remanent magnetization as the system evolves into the ordered bulk AFM phase below Néel temperature $T_{\mathrm{N}} \approx 13$ K.

The observed temperature-driven transition points to an underlying exchange competition that requires quantifying the Mn_{Sb} antisite defect density. As shown in Fig. 1d, high-field pulsed magnetometry up to 56 T was employed to isolate these defect contributions, with the pulsed-field measurements calibrated against superconducting quantum interference device (SQUID) data in the low-field overlap region. In the low-field regime at 2 K, the magnetization reaches a plateau of $M_1 \approx 1.9\ \mu_{\mathrm{B}}$/f.u.. We attribute

this reduced magnetic moment to the antiparallel coupling between the host Mn_{Mn} spins and the interlayer Mn_{Sb} defects (mediated by J^2_{AFM}), which generates a ferrimagnetic net moment expressed as $M_1 = M_{main} - M_{defect}$ [20,31]. When the external pulsed field is increased into the ultra-high regime, a magnetization plateau emerges above 55 T, yielding a saturation magnetization of $M_2 \approx 6.5\ \mu_B$/f.u., which corresponds to a completely polarized state where all Mn moments align parallel to the magnetic field $M_2 = M_{main} + M_{defect}$. Through the decoupling of these two distinct field-driven regimes, the relative fraction of misallocated spins within the total magnetic network (x) can be mathematically isolated via: $x = \frac{M_{defect}}{M_2} = \frac{M_2 - M_1}{2M_2}$. This evaluation yields an effective magnetic fraction of $x \approx 0.354$, corresponding to a chemical stoichiometry of $(Mn_{1-x}Sb_x)(Sb_{6-x}Mn_x)Te_{10}$ under strict conservation of the total magnetic mass.

Because the apparent high-field moment, $M_2 \approx 6.5\ \mu_B$/f.u., exceeds the spin-only value expected for an isolated high-spin Mn^{2+} ion, the estimated Mn_{Sb}-related contribution should be interpreted as an effective magnetic fraction rather than a direct crystallographic antisite occupancy. And this excess may partly arise from additional contributions to the measured high-field magnetization, such as a possible ferromagnetic MnSb secondary phase and a field-dependent paramagnetic background. This effective estimate nevertheless points to a strongly site-mixed magnetic lattice, providing a material basis for the defect-sensitive FM–AFM competition and motivating a real-space examination of the low-temperature FM state.

3. MFM imaging

Direct real-space magnetic imaging is vital for elucidating the relationship between the microscopic distribution of antisite defects and local domain reversal dynamics [27,32–35]. MFM measurements were conducted on the pristine cleavage surface of $MnSb_6Te_{10}$ at a base temperature of 1.7 K with a fixed tip lift height of 200 nm (Fig. 2a). Initial polarization at −0.10 T establishes a stable, downward-aligned M^- state that persists at 0 T, characterizing a single-domain remanent FM configuration. A distinct region (white dashed box) displays diminished FM contrast at zero field; this suggests locally attenuated ferromagnetism, likely resulting from a deficient local density of Mn_{Sb} antisite defects.

Sweeping the field to positive values reveals M^+ domain nucleation near +0.016 T as isolated high-frequency contrast features. As the field increases, these nuclei expand and merge through domain-wall motion, with the scanned region reaching a nearly switched state by +0.022 T. The domain fragmentation is most pronounced near the coercive field, a trend quantified by the RMS frequency roughness which exhibits a distinct maximum at +0.021 T (Fig. 2c). We estimate M/M_s from the MFM images using a two-state domain model. The normalized RMS contrast reaches its maximum when oppositely magnetized domains occupy approximately equal areas and decreases as either orientation becomes dominant; this contrast is converted into the magnitude of M/M_s. Its sign is assigned from the mean MFM signal using the saturated images as polarity references. The detailed calculation is provided in the Supporting Information S1. While the local magnetization curve reconstructed from MFM contrast is qualitatively

consistent with the bulk SQUID loop (Fig. 2b), the quantitative discrepancies underscore the sensitivity of the reversal process to lateral fluctuations in defect density. Notably, the region marked by the dashed box exhibits delayed switching; this confirms a locally suppressed FM state. These measurements collectively demonstrate that the low-temperature magnetic state is a reversibly switchable FM phase characterized by nanoscale magnetic inhomogeneity (see Supplementary Fig. S1 for complete MFM sequences and analysis).

To investigate the real-space dynamics of the thermal FM-to-AFM transition, temperature-dependent MFM imaging was conducted under zero external field, as shown in Fig. 3a. The domain pattern was prepared at 1.7 K by polarizing the sample at -0.10 T, stepping forward to $+0.016$ T to maximize domain contrast, and reducing back to 0 T. During heating, the MFM tip was maintained at a constant lift height of 600 nm to suppress tip-induced magnetic perturbations, ensuring a purely thermally driven spin reorientation.

To quantify the thermal relaxation process, the RMS magnetic signal (frequency shift δf) was extracted from the MFM images and plotted as the purple curve in Fig. 3b. The temperature dependence of δf_{rms}, which scales with the spatial variance of local magnetic stray fields, reveals a multi-stage relaxation profile. During the initial warming stage, the roughness remains nearly constant, indicating that the local pinning potential from the dense $\mathrm{Mn_{Sb}}$ antisite network stabilizes the remanent FM order against mild thermal fluctuations. Upon further warming, the stray-field landscape is rapidly suppressed within a narrow temperature window between 2.3 and 4.0 K. In this regime, the continuous FM textures fragment into microscale magnetic islands—a clear signature of first-order phase transition behavior characterized by the coexistence of FM and AFM domain textures. Above 4.0 K, the MFM contrast vanishes, consistent with the loss of the field-prepared FM state and the emergence of a more compensated magnetic configuration. The 12 Kmagnetization curve retains a field-dependent plateau, whereas the 15 K curve is paramagnetic-like Fig. 1c, supporting the presence of magnetic order in the intermediate-temperature regime. This morphological evolution is quantitatively supported by domain-counting, area-fraction, and fractal-dimension analyses (Supplementary Fig. S2). These observations demonstrate that thermal fluctuations in this range overcome the local pinning barrier, causing the extended FM texture to lose spatial coherence and relax via first-order fragmentation toward the compensated AFM ground state.

At higher temperatures, the MFM frequency contrast flattens further and approaches the MFM noise floor. The temperature-dependent RMS roughness (purple curve in Fig. 3b) closely tracks the suppression of the zero-field remanent magnetization measured by SQUID (red curve). Because this contrast loss occurs well below the bulk Néel temperature ($T_{\mathrm{N}} \approx 13$ K), it signifies the extinction of the metastable FM order rather than a transition to a paramagnetic (PM) state. This homogeneous low-contrast MFM landscape is therefore consistent with the recovery of the compensated AFM ground state, where the net stray field is strongly suppressed. Collectively, the magnetization and MFM observations are consistent with relaxation from the field-prepared FM state toward an AFM- dominant state below the magnetic ordering temperature, as also supported by the negative interlayer correlations in the Monte Carlo model.

4. MC simulations

To rationalize this relaxation pathway, we performed classical MC simulations using a minimal layered spin model. We employed a $32 \times 32 \times 2$ lattice with intralayer FM coupling and site-dependent interlayer exchange. Pristine regions favor AFM interlayer alignment, whereas defect sites introduce FM-favored exchange paths. The Hamiltonian of the system is expressed as:

$$\mathcal{H} = -J_{\text{in}} \sum_{\langle i,j \rangle,\gamma} \mathbf{S}_{i,\gamma} \cdot \mathbf{S}_{j,\gamma} - \sum_{i} J_{\text{out}}(i)\, \mathbf{S}_{i,1} \cdot \mathbf{S}_{i,2} - \sum_{i,\gamma} K (S^{z}_{i,\gamma})^2 \tag{1}$$

where $\mathbf{S}_{i,\gamma}$ is the three-dimensional normalized classical spin vector at site i on layer $\gamma = 1, 2$. The parameter $J_{\text{in}} = 1.0$ represents the intrinsic intralayer nearest-neighbor FM exchange coupling. To model the experimental magnetic disorder, we introduced a spatially inhomogeneous interlayer coupling $J_{\text{out}}(i)$: pristine sites are coupled via the native AFM interaction ($J_{\text{out}} = -0.10$), while at randomly distributed Mn_{Sb} antisite locations (with defect concentration p_{d}), this is replaced by a local FM interaction ($J_{\text{out}} = 0.08$). The final term accounts for the easy-axis single-ion anisotropy ($K = 0.10$) along the z-axis. All parameters are given in dimensionless units. The simulations were initialized from a fully polarized FM state and thermally evolved to mimic field-prepared sample warming.

Because $|J_{\text{in}}| \gg |J_{\text{out}}|$, the intralayer ferromagnetic order is significantly more robust than the interlayer interactions. This hierarchy suppresses atomic-scale phase separation, effectively forcing the layers to behave as collective macro-moments. Consequently, the system stabilizes in either a global FM- or AFM-dominant state, with the transition between them tuned by the defect density p_{d}. This competitive magnetic landscape is represented by the energy schematic in Fig. 4c, where the intrinsic AFM configuration resides at the global energy minimum, while the defect-driven FM order acts as a metastable local minimum. Field polarization prepares the system in the metastable FM state, and subsequent thermal activation provides the pathway to escape this energy well and relax into the intrinsic AFM ground state.

To identify the magnetic phases, we utilized the interlayer spin correlation function, defined as $C_{\text{inter}} = \langle \mathbf{S}_{i,1} \cdot \mathbf{S}_{i,2} \rangle$. This metric serves as a phenomenological indicator of the interlayer magnetic alignment: positive and negative values signify FM- and AFM-dominant correlations, respectively, while values approaching zero reflect a thermally disordered, PM-like state.

We used C_{inter} to track the thermal evolution of the FM-initialized state at a representative defect fraction of $p_{\text{d}} = 35\%$. As shown in Fig. 4h, C_{inter} is positive at low temperatures, reflecting the FM-dominant interlayer order inherited from the initial state. Warming the system leads to an abrupt sign reversal of C_{inter} near $T \approx 0.51$, marking a crossover from FM- to AFM-dominant correlations. This sharp transition is a characteristic signature of a first-order phase transition, consistent with the spatial domain coexistence observed in our MFM experiments. At higher temperatures ($T \approx 0.8$), C_{inter} asymptotically approaches zero, indicating that thermal fluctuations have suppressed the magnetic order into a disordered, PM-like phase.

Figure 4d–g presents the real-space evolution of the lattice. Fig. 4d displays the defect map, with black sites representing FM-favored interlayer exchange channels embedded within the native AFM background.

Figs. 4e–g visualize the spatial distribution of the local interlayer spin correlation ($\mathbf{S}_{i,1} \cdot \mathbf{S}_{i,2}$) at $p_{\mathrm{d}} = 35\%$ across selected temperatures. Using a color scale where yellow signifies local FM interlayer alignment ($C_{\mathrm{inter}} \approx 1$) and dark blue indicates local AFM alignment ($C_{\mathrm{inter}} \approx -1$), we observe a clear transition: at $T = 0.10$, the system maintains a single-domain FM-dominant state; by $T = 0.53$, it has effectively switched to an AFM-dominant configuration; at $T = 1.0$, the distribution becomes randomized, reflecting the loss of interlayer correlations in the disordered PM-like phase.

The dependency on defect density is summarized in Fig. 4i, mapping $C_{\mathrm{inter}}(T)$ across varying p_{d}. At low defect densities, the system remains in an AFM-dominant state at low temperatures, whereas high defect densities stabilize the FM order up to the PM transition. In the intermediate regime ($p_{\mathrm{d}} \approx 20\%$–$50\%$), the system enters a competitive landscape where the field-prepared FM state is metastable and becomes unstable upon warming (see Supplementary Fig. S3). Here, relaxation occurs via a spatially fragmented intermediate texture before the recovery of AFM-dominant correlations. This establishes a microscopic mechanism where spatially inhomogeneous defect-mediated exchange traps the system in a metastable FM state, with thermal activation facilitating the transition to the AFM ground state.

5. Conclusion

In conclusion, we have resolved the real-space dynamics of the defect-driven FM-to-AFM phase transition in the vdW superlattice $MnSb_6Te_{10}$, identifying cation site-mixing as a deterministic parameter for tuning the underlying magnetic energy landscape. Our analysis demonstrates that the defect density (p_{d}) acts as a critical control knob: the concentration of Mn_{Sb} antisite defects dictates the stability of the metastable FM state, with an optimal defect window facilitating the tunable FM-to-AFM relaxation observed here. High-field magnetization measurements quantified this site-mixing, while cryogenic MFM provided real-space evidence of a metastable FM state sustained by defect-mediated interlayer interactions. Temperature-dependent MFM further captured the first-order thermal relaxation process, where continuous FM domains fragment into microscopic islands before the system recovers its intrinsic, compensated AFM state—a mechanism corroborated by our spatially inhomogeneous Heisenberg model simulations.

Crucially, these findings establish that controlling defect density offers a viable framework for manipulating magnetic symmetry in topological materials. At low temperatures, the defect-stabilized FM alignment breaks time-reversal symmetry, creating a state compatible with Weyl semimetal or Chern insulator phases. Upon warming into the intrinsic AFM state, the restoration of combined time-reversal and inversion symmetry ($\mathcal{PT}$) sets up a baseline for axion insulating behavior [3,25,36]. The energetic proximity between these distinct magnetic configurations, coupled with their sensitivity to defect-mediated exchange, provides an encouraging blueprint for dynamically gating non-trivial quantum states. By leveraging structural site-mixing as a tuning parameter, our work points toward customizable, nanoscale spin-topology device architectures.

Appendix A: Experimental methods

Crystal growth

High-quality single crystals of $MnSb_6Te_{10}$ were grown using a self-flux method. High-purity Mn pieces (Macklin, 99.999%), Sb powders (Macklin, 99.999%), and Te powders (Macklin, 99.999%) were mixed in a molar ratio of 1:8:13, loaded into an evacuated quartz tube, and sealed. The mixture was heated to 973 K, held for 10 hours, then cooled to 898 K over 10 hours, followed by further cooling to 873 K over another 10 hours, after which the melt was rapidly centrifuged. This yielded single crystals with typical dimensions of $3 \times 3 \times 0.1\,\mathrm{mm}^3$ at the bottom of the crucible.

Bulk magnetization measurements

The low-field bulk magnetizations were measured by using a commercial Magnetic Property Measurement System (MPMS-3).Pulsed-field magnetization was performed at the Wuhan National High Magnetic Field Center (WHMFC) in a 65 T magnet with a pulse duration time of 10 ms. Magnetization was measured by a standard induction method using a compensated coaxial pick-up coil, during which the induced voltage was integrated over time to obtain the magnetization. The absolute values of magnetization were calibrated against low-field data measured in the MPMS-3 SQUID magnetometer.

MFM measurements

MFM images were acquired using a commercial cryogenic AFM system (Attodry2100) with commercial magnetic probes (resonance frequency ≈ 75 kHz, force constant ≈ 2.8 N/m). The MFM signal, which corresponds to the change in cantilever resonant frequency, is proportional to the out-of-plane stray field gradient. Electrostatic interactions were minimized by nulling the tip–surface contact potential difference. Field-dependent MFM images were acquired at a lift height of 200 nm to resolve domain nucleation and reversal. Temperature-dependent images were acquired at 600 nm to reduce perturbation of the magnetic state by the MFM tip during warming.

Acknowledgement

Wenbo Wang was sponsored by National Natural Science Foundation of China (Grant No. 12374161), and National Key Research and Development Program of China (Grant No. 2025YFA1412100 and No. 2022YFA1403000). Yanfeng Guo was sponsored by Analytical Instrumentation Center (#SPST-AIC10112914) and the Double First-Class Initiative Fund of ShanghaiTech University. This work was supported by Magnetic Property Station of the Wuhan National High Magnetic Field Center(https://whmfc.hust.edu.cn/yhfw/cljs.htm).

参考文献

[1] Chang C Z, Zhang J, Feng X, Shen J, Zhang Z, Guo M, Li K, Ou Y, Wei P, Wang L L, Ji Z Q, Feng Y, Ji S, Chen X, Jia J, Dai X, Fang Z, Zhang S C, He K, Wang Y, Lu L, Ma X C and Xue Q K 2013 *Science* **340** 167–170

[2] Tokura Y, Yasuda K and Tsukazaki A 2019 *Nat. Rev. Phys.* **1** 126–143

[3] Zhang D, Shi M, Zhu T, Xing D, Zhang H and Wang J 2019 *Phys. Rev. Lett.* **122** 206401

[4] Deng Y, Yu Y, Shi M Z, Guo Z, Xu Z, Wang J, Chen X H and Zhang Y 2020 *Science* **367** 895–900

[5] Li J, Li Y, Du S, Wang Z, Gu B L, Zhang S C, He K, Duan W and Xu Y 2019 *Sci. Adv.* **5** eaaw5685

[6] Gong Y, Guo J, Li J, Zhu K, Liao M, Liu X, Zhang Q, Gu L, Tang L, Feng X, Zhang D, Li W, Song C, Wang L, Yu P, Chen X, Wang Y, Yao H, Duan W, Xu Y, Zhang S C, Ma X, Xue Q K and He K 2019 *Chin. Phys. Lett.* **36** 076801

[7] Otrokov M M, Rusinov I P, Blanco-Rey M, Hoffmann M, Vyazovskaya A Y, Eremeev S V, Ernst A, Echenique P M, Arnau A and Chulkov E V 2019 *Phys. Rev. Lett.* **122** 107202

[8] Klimovskikh I I, Otrokov M M, Estyunin D, Eremeev S V, Filnov S O, Koroleva A, Shevchenko E, Voroshnin V, Rybkin A G, Rusinov I P, Blanco-Rey M, Hoffmann M, Aliev Z S, Babanly M B, Amiraslanov I R, Abdullayev N A, Zverev V N, Kimura A, Tereshchenko O E, Kokh K A, Petaccia L, Di Santo G, Ernst A, Echenique P M, Mamedov N T, Shikin A M and Chulkov E V 2020 *npj Quantum Mater.* **5** 54

[9] Vyazovskaya A Y, Bosnar M, Chulkov E V and Otrokov M M 2025 *Commun. Mater.* **6** 88

[10] Wang Y, Fu B, Wang Y, Lian Z, Yang S, Li Y, Xu L, Gao Z, Yang X, Wang W, Jiang W, Zhang J, Wang Y and Liu C 2025 *Nat. Commun.* **16** 1727

[11] Lian Z, Wang Y, Wang Y, Dong W H, Feng Y, Dong Z, Ma M, Yang S, Xu L, Li Y, Fu B, Li Y, Jiang W, Xu Y, Liu C, Zhang J and Wang Y 2025 *Nature* **641** 70–75 ISSN 1476-4687

[12] Hu C, Gordon K N, Liu P, Liu J, Zhou X, Hao P, Narayan D, Emmanouilidou E, Sun H, Liu Y, Brawer H, Ramirez A P, Ding L, Cao H, Liu Q, Dessau D and Ni N 2020 *Nat. Commun.* **11** 97

[13] Xi M and Lei H 2024 *Chin. Phys. B* **33** 067503

[14] Eremeev S V, Rusinov I P, Koroteev Y M, Vyazovskaya A Y, Hoffmann M, Echenique P M, Ernst A, Otrokov M M and Chulkov E V 2021 *J. Phys. Chem. Lett.* **12** 4268–4277

[15] Guo J, Wang H, Zhang H, Mi S, Li S, Dong H, Zhu S, Hu J, Wang X, Li Y, Sugawara Y, Xu R, Pang F, Ji W, Xia T and Cheng Z 2024 *Phys. Rev. B* **109** 174431

[16] Liu Y, Wang L L, Zheng Q, Huang Z, Wang X, Chi M, Wu Y, Chakoumakos B C, McGuire M A, Sales B C, Wu W and Yan J 2021 *Phys. Rev. X* **11** 021033

[17] Xi M, Chen F, Gong C, Tian S, Yin Q, Qian T and Lei H 2022 *J. Phys. Chem. Lett.* **13** 10897–10904

[18] Xiong J, Peng Y H, Lin J Y, Cen Y J, Yang X B and Zhao Y J 2023 *Materials* **16** 5496

[19] Hu X, He X, Guo Z, Kamiya T and Wu J 2024 *ACS Nano* **18** 738–749

[20] Chen H, Wang J, Li H, Duan X, Wang Y, Xu Z, Xia Y, He W, Jia Z, Cao X, Mou Y, Jiang X, Gu J, Leng P, Zhu F, Zheng C, Yuan X, Xiu F, Zhou T, Miao L and Zhang C 2026 *Nat. Commun.* **17** 1029

[21] Zhang J, Xi M, Zhang Y, Li H, Zhao J, Lei H, Wei Z and Qian T 2025 *Chin. Phys. B* **34** 076801

[22] Huan S, Zhang S, Jiang Z, Su H, Wang H, Zhang X, Yang Y, Liu Z, Wang X, Yu N, Zou Z, Shen D, Liu J and Guo Y 2021 *Phys. Rev. Lett.* **126** 246601

[23] Xu X, Yang S, Wang H, Guzman R, Gao Y, Zhu Y, Peng Y, Zang Z, Xi M, Tian S, Li Y, Lei H, Luo Z, Yang J, Wang Y, Xia T, Zhou W, Huang Y and Ye Y 2022 *Nat. Commun.* **13** 7646

[24] Yan C, Zhu Y, Miao L, Fernandez-Mulligan S, Green E, Mei R, Tan H, Yan B, Liu C X, Alem N, Mao Z and Yang S 2022 *Nano Lett.* **22** 9815–9822

[25] Zhang X, Zhang S, Jiang Z, Yang Y, Liu Z, Yang S, Jiao J, Yu L, Xia W, Wang X, Yu N, Zou Z, Ma J, Liu Y, Shen D, Liu J and Guo Y 2025 *Phys. Rev. Mater.* **9** 044201

[26] Xi M, Zhang Y, Zhou W, Chen F, Jia D, Gou H, Qian T and Lei H 2025 *J. Phys. Chem. Lett.* **16** 9507–9516

[27] Ge W, Kim J, Chan Y T, Vanderbilt D, Yan J and Wu W 2022 *Phys. Rev. Lett.* **129** 107204

[28] Yuan Y, Wang X, Li H, Li J, Ji Y, Hao Z, Wu Y, He K, Wang Y, Xu Y, Duan W, Li W and Xue Q K 2020 *Nano Lett.* **20** 3271–3277

[29] Garnica M, Otrokov M M, Casado Aguilar P, Klimovskikh I I, Estyunin D, Aliev Z S, Amiraslanov I R, Abdullayev N A, Zverev V N, Babanly M B, Mamedov N T, Shikin A M, Arnau A, Vázquez de Parga A L, Chulkov E V and Miranda R 2022 *npj Quantum Mater.* **7** 7

[30] Lüpke F, Kolmer M, Yan J, Chang H, Vilmercati P, Weitering H H, Ko W and Li A P 2023 *Commun. Mater.* **4** 82

[31] Lai Y, Ke L, Yan J, McDonald R D and McQueeney R J 2021 *Phys. Rev. B* **103** 184429

[32] Sass P M, Ge W, Yan J, Obeysekera D, Yang J J and Wu W 2020 *Nano Lett.* **20** 2609–2614

[33] Sass P M, Kim J, Vanderbilt D, Yan J and Wu W 2020 *Phys. Rev. Lett.* **125** 037201

[34] Webb T A, Tamanna A N, Ding X, Verma N, Xu J, Krusin-Elbaum L, Dean C R, Basov D N and Pasupathy A N 2024 *Nano Lett.* **24** 4393–4399

[35] Shi Y, Bai Y, Li Y, Feng Y, Li Q, Zhang H, Chen Y, Tong Y, Luan J, Liu R, Ji P, Gao Z, Guo H, Zhang J, Wang Y, Feng X, He K, Zhou X and Shen J 2024 *Phys. Rev. Mater.* **8** 124202

[36] Hu C, Ding L, Gordon K N, Ghosh B, Tien H J, Li H, Linn A G, Lian S W, Huang C Y, Mackey S, Liu J, Reddy P V S, Singh B, Agarwal A, Bansil A, Song M, Li D, Xu S Y, Lin H, Cao H, Chang T R, Dessau D and Ni N 2020 *Sci. Adv.* **6** eaba4275

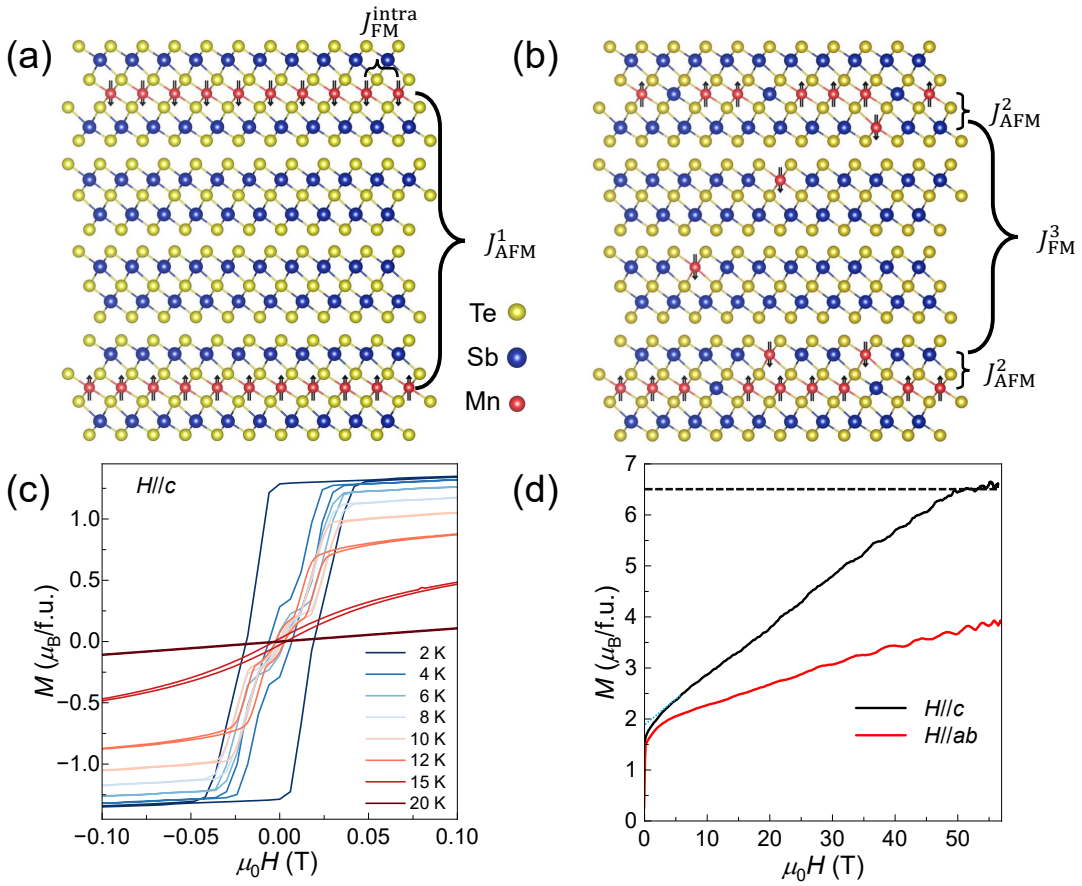


图 1: Defect-sensitive FM–AFM competition in $MnSb_6Te_{10}$. (a) Ideal layered structure of $MnSb_6Te_{10}$, consisting of one magnetic $MnSb_2Te_4$ septuple layer separated by two nonmagnetic Sb_2Te_3 quintuple layers. The intralayer FM exchange $J_{\mathrm{FM}}^{\mathrm{intra}}$ aligns Mn moments within each septuple layer, whereas the native interlayer AFM coupling J_{AFM}^{1} favors antiparallel alignment between neighboring magnetic layers. (b) Schematic structure containing Mn_{Sb} antisite defects. Defect moments located in the spacer region introduce additional exchange pathways, including local Mn_{Mn}–Mn_{Sb} coupling J_{AFM}^{2} and defect-mediated FM correlations J_{FM}^{3}, which can compete with the native interlayer AFM coupling. (c) Temperature-dependent M–H loops measured with the magnetic field applied along the c axis. A remanent FM-like response appears at low temperature and is suppressed upon warming within the AFM-ordered regime. (d) Pulsed-field magnetization measured up to 56 T at 2 K. Within an effective ferrimagnetic decomposition model, the low-field and high-field magnetization plateaus, M_1 and M_2, are used to estimate an effective Mn_{Sb} antisite population of approximately 35.4%.

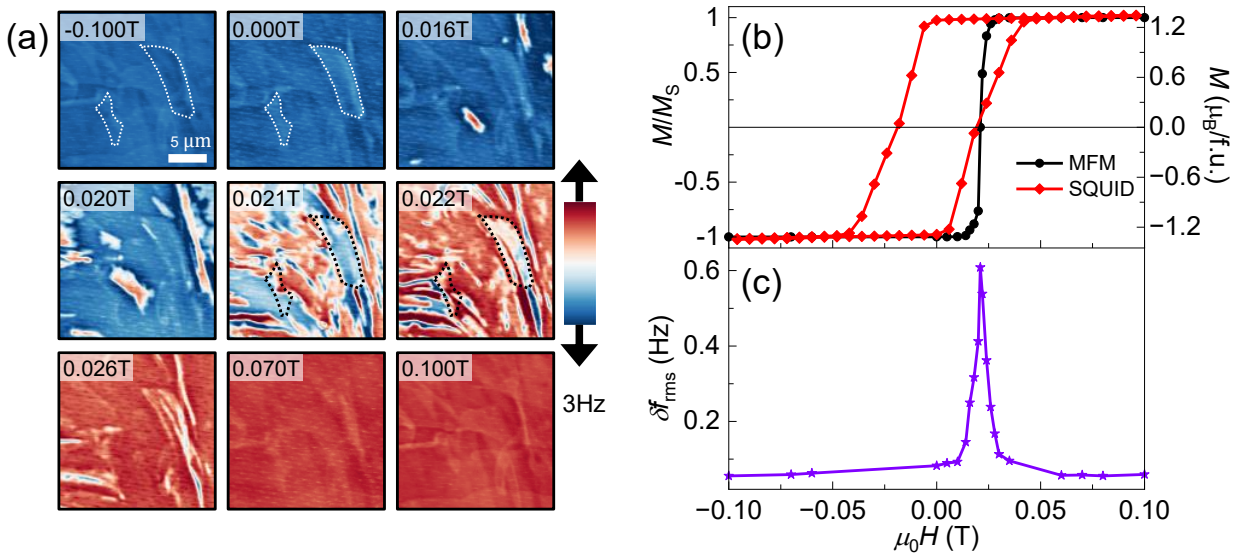


图 2: Magnetization reversal of the metastable FM state at 1.7 K. (a) Cryogenic MFM images of $MnSb_6Te_{10}$ measured at 1.7 K under an out-of-plane magnetic field swept from −0.10 T to +0.10 T. After initialization at −0.10 T, the magnetic contrast is retained at zero field, indicating a remanent single-domain-like M^- configuration. Upon sweeping to positive fields, reversed M^+ domains nucleate, expand, and merge until nearly complete reversal. The dashed box marks a region with reduced contrast at zero field and delayed switching, suggesting local magnetic inhomogeneity. The color scale is 3 Hz, and the scale bar is 5 μm. (b) Normalized local magnetization M/M_s reconstructed from the MFM contrast and compared with the bulk magnetization loop at 2 K. The two measurements give consistent switching behavior, with a coercive field of approximately 0.021 T. (c) RMS frequency roughness extracted from the MFM images as a function of magnetic field, showing a maximum near +0.021 T where half of the magnetization is reversed.

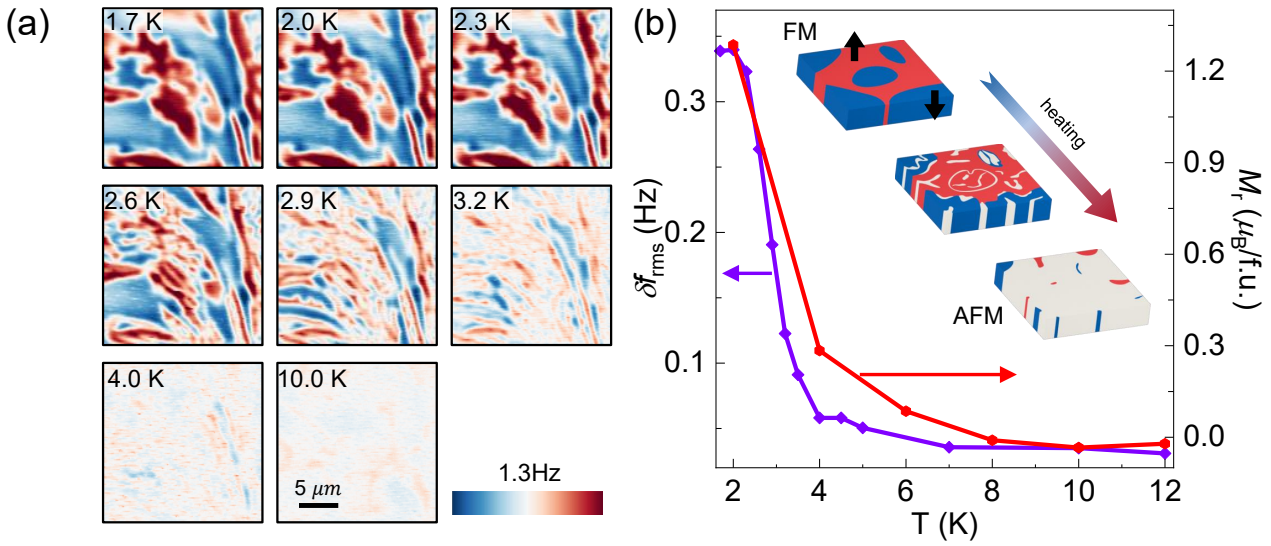


图 3: Zero-field thermal fragmentation of the field-prepared FM state. (a) Temperature-dependent MFM images acquired at zero external field after preparing a remanent FM multidomain state at 1.7 K. The initial state was prepared by polarizing the sample at −0.10 T, sweeping to +0.016 T to generate strong domain contrast near the reversal regime, and returning to zero field before warming. Upon warming, the extended FM domains progressively fragment into smaller regions, the MFM contrast weakens, and the image eventually becomes nearly homogeneous. Since this evolution occurs below the Néel temperature, the loss of stray-field contrast is consistent with relaxation toward a compensated AFM configuration rather than a paramagnetic transition. The color scale is 1.3 Hz, the scale bar is 5 μm, and the lift height is 600 nm. (b) Temperature dependence of the RMS frequency roughness extracted from the MFM images, compared with the zero-field remanent magnetization measured by SQUID. The inset schematic demonstrates the domain fragmentation during the FM-to-AFM phase transition.

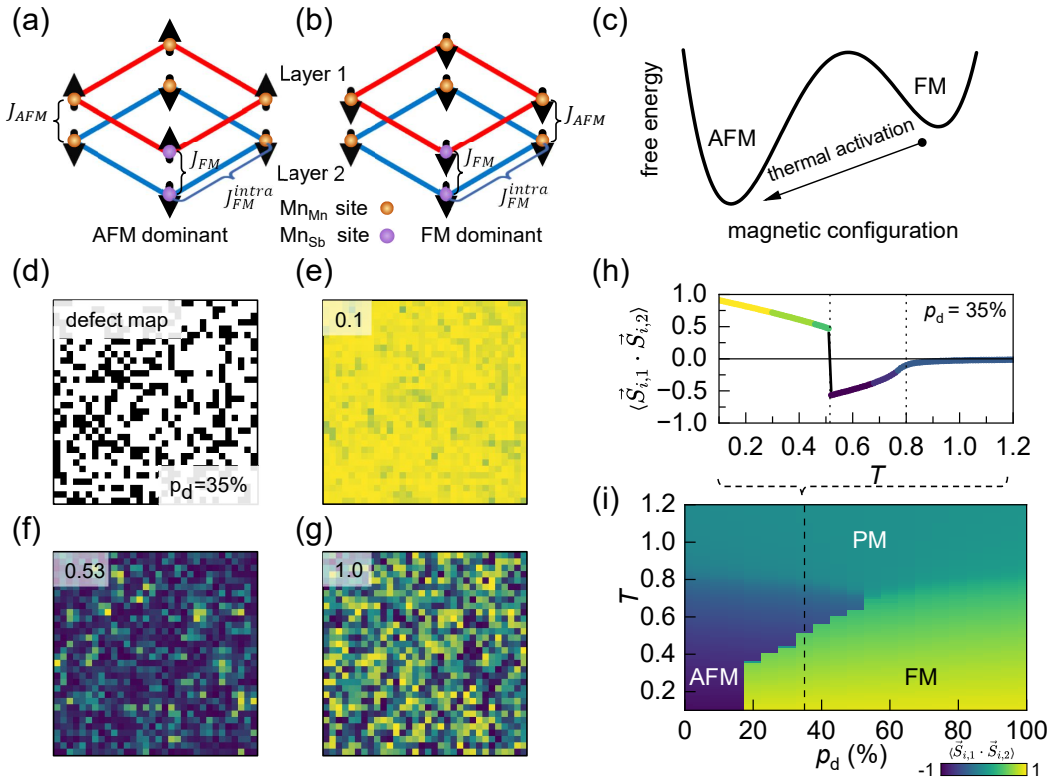


图 4: Monte Carlo simulation of metastable FM relaxation. (a,b) Schematic spin configurations generated within the same competing interlayer exchange framework. The model includes intralayer FM exchange, native interlayer AFM coupling, and defect-mediated exchange pathways associated with Mn_{Sb} antisite sites. Under the same set of competing interactions, the system can exhibit either (a) an AFM-dominant configuration or (b) an FM-dominant configuration, depending on the resulting balance of interlayer correlations. (c) Schematic magnetic energy landscape as a function of magnetic configuration or interlayer correlation. The AFM-favored configuration is represented as the global energy minimum, whereas the defect-associated FM configuration is represented as a metastable minimum. Thermal activation provides a possible pathway for relaxation from the metastable FM configuration toward the AFM ground state. (d) Representative defect map used in the simulation with a defect concentration of $p_d = 35\%$. (e–g) Spatial maps of the simulated interlayer spin dot product at representative temperatures $T = 0.10$, 0.53, and 1.00, respectively. The simulation is initialized from a fully polarized FM single-domain state to mimic the field-prepared state in the MFM experiment. Upon warming, the initially FM-dominant interlayer correlation becomes spatially fragmented and evolves toward AFM-dominant correlations; at higher temperature, the correlation becomes strongly reduced and spatially disordered. (h) Temperature dependence of the averaged interlayer spin correlation, C_{inter}, at $p_{\text{d}} = 35\%$. This curve shows a crossover from a defect-associated FM-dominant configuration to an AFM-dominant configuration, followed by a reduction of the averaged interlayer correlation at higher temperature. (i) Simulated temperature dependence at different defect density of the averaged interlayer spin correlation, C_{inter}. The black dashed line marks $p_{\text{d}} = 35\%$, corresponding to the line cut shown in panel (h).